Journal of Materials Chemistry A

Accepted Manuscript

ROYAL SOCIETY OF CHEMISTRY

www.rsc.org/materialsA

Table of Contents

An efficient hybrid organic-inorganic H_2 evolving photocathode, consisting of donor/acceptor polymeric blend, inorganic charge-selective layers and Pt electrocatalyst is demonstrated. It yields 100% faradaic efficiency, photocurrent densities of 3mAcm^{-2} at 0.0V RHE and onset potentials of +0.67V RHE. Roles and stability of the system interfaces are investigated, organic semiconductors are proven to be a stable photocathode material. This work establishes organic semiconductors as a radically new option for efficient direct conversion of solar energy into fuels.

Keywords: hybrid organic inorganic photocathodes; hydrogen evolution; semiconducting polymer; P3HT:PCBM; charge selective interfacial layers

F. Fumagalli, S. Bellani, M. Schreier, S. Leonardi, H. Comas Rojas, A. Ghadirzadeh, G. Tullii, A. Savoini, G. Marra, L. Meda, M. Grätzel, G. Lanzani, M. T. Mayer, M. R. Antognazza* and F. Di Fonzo*.

Hybrid organic-inorganic H_2-evolving photocathodes: understanding the route towards high performances organic photoelectrochemical water splitting

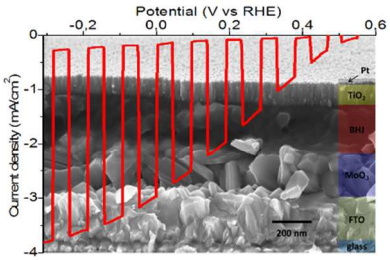

Journal Name

ARTICLE

Hybrid organic-inorganic H_2-evolving photocathodes: understanding the route towards high performances organic photoelectrochemical water splitting.

Received 00th January 20xx,
Accepted 00th January 20xx

DOI: 10.1039/x0xx00000x

www.rsc.org/

Francesco Fumagalli[a‡], Sebastiano Bellani[a‡], Marcel Schreier[b], Silvia Leonardi[a], Hansel Comas Rojas[a], Alì Ghadirzadeh[a], Gabriele Tullii[a], Alberto Savoini[c], Gianluigi Marra[c], Laura Meda[c], Michael Grätzel[b], Guglielmo Lanzani[a], Matthew T. Mayer[b], Maria Rosa Antognazza[a]* and Fabio Di Fonzo[a]*

A promising, yet challenging, route towards renewable production of hydrogen is the direct conversion of solar energy at a simple and low cost semiconductor/water junction. Despite the theoretical simplicity of such a photoelectrochemical device, different limitations among candidate semiconductor materials have hindered its development. After many decades of research on inorganic semiconductors, a conclusive solution still appears out of reach. Here, we report an efficient hybrid organic-inorganic H_2 evolving photocathodes, consisting of a donor/acceptor blend sandwiched between charge-selective layers and a thin electrocatalyst layer. The role and stability of the different interfaces are investigated, and the conductive polymer is proven to be an efficient material for a semiconductor/liquid PEC junction. The best performing electrodes show high performances with a photocurrent of 3 mA/cm^2 at 0 V vs RHE, optimal process stability with 100% faradaic efficiency during electrode's lifetime, excellent energetics with +0.67 V vs RHE onset potential, promising operational activity of several hours and by-design compatibility for implementation in a tandem architecture. This work demonstrates organic semiconductors as a radically new option for efficient direct conversion of solar energy into fuels, and points out the route towards high performances organic photoelectrochemical water splitting.

Introduction

Direct conversion of solar energy into fuels is crucial for sustainable development and offers the prospect of establishing a carbon-neutral energy cycle.[1] A photoelectrochemical (PEC) cell is a potentially low cost and scalable system in which, driven by sunlight, water is split directly into hydrogen and oxygen at a semiconductor/liquid junction. [2] Thermodynamically, the minimal voltage required to split water is 1.23 V ($\Delta G°$ = 475 kJ mol^{-1}) at standard conditions, whereas in practical systems several non-idealities (e.g. electrocatalytic overpotentials and series resistances) increase this requirement upwards of 1.5 V. This energetic constraint and the need for efficient use of the solar spectrum suggest an ideal device based on a dual light absorber, or tandem, configuration. Stacking a 1.6–1.8 eV band gap semiconductor above a smaller (ca. 1 eV) band gap material, like Si, promises a route toward optimum solar-to-hydrogen efficiencies. [3, 4] Extensive research has been performed, primarily on inorganic metal oxides, toward designing an efficient, stable, and earth-abundant wide band gap photoelectrode to use as the top component. Nevertheless, no ideal material has yet been identified. Thus an urgent need exists to explore new types of materials for photoelectrochemical water splitting. In this view, semiconducting polymers (SP) represent an attractive, yet largely unexplored, class of materials. Recently, Sprick et al. demonstrated the potential of organic semiconductors as photocatalysts for H_2 production under visible light. [5] SPs can exhibit either p- or n-type character, offer tunable band gaps and energy levels [6] and are easily scalable to large area applications by means of roll-to-roll printing. [7] Since SPs are characterized by Lowest Unoccupied Molecular Orbital (LUMO) energy levels several hundreds of millivolts negative of the hydrogen evolution potential, these materials are excellent candidates to act as photocathodes driving various reduction reactions [8,9]. As an example, the prototypical conjugated polymer used in organic photovoltaics, the electron-donating regioregular Poly(3-hexylthiophene-2,5-diyl) (rr-P3HT), has a direct bandgap of 1.9 eV, close to the optimum for a PEC tandem device, and capable of delivering a record

[a.] Center for Nano Science and Technology @PoliMi, Istituto Italiano di Tecnologia, Via Pascoli 70/3, 20133 Milano, Italy..
[b.] Laboratory of Photonics and Interfaces, Institute of Chemical Sciences and Engineering, Ecole Polytechnique Fédérale de Lausanne, CH-1015 Lausanne, Switzerland
[c.] . Eni S.p.A., Istituto ENI Donegani, Via Giacomo Fauser 4, 28100 Novara, Italy.
† These authors contributed equally.
E-mail: fabio.difonzo@iit.it; mariarosa.antognazza@iit.it
Electronic Supplementary Information (ESI) available: See DOI: 10.1039/x0xx00000x

photocurrent density (under 1 sun illumination) of up to 14 mA cm^{-2} (obtained with an organic solar cell). [10] The same rationale also applies to donor-acceptor blends since typical organic acceptors have LUMO levels negative of the hydrogen evolution potential, thereby allowing for the design of photocathodes based on the bulk heterojunction (BHJ) architecture.[11] Furthermore, it was recently shown that rr-P3HT fully retains its optoelectronic properties, particularly in terms of charge generation efficiency, in an aqueous environment. [12, 13] Overall, these characteristics suggest that it is conceivable to exploit semiconducting polymers to reach sunlight-to-hydrogen conversion efficiencies over 10% (based on the AM1.5 spectrum and the low heating value of hydrogen). Despite their appealing features, however, SPs have drawn little attention for application in PEC devices and reported performances for basic architectures remained low, i.e. exhibiting photocurrent densities in the sub-mA/cm^2 region, [9,14]in comparison to their inorganic counterparts both in terms of efficiency [15] and stability [16]. Recent reports about photocathodes for hydrogen evolution and SPs, describing more sophisticated architectures, manage to overcome the threshold of 1 mA cm^{-2} photogenerated current density at positive bias, approaching the realm of inorganic systems based on comparable band gap absorbers with similar theoretical solar-to-fuel efficiency. Lai et al. [17] demonstrated a fully transparent photocathode based on a NP-CdSe/P3HT type II bulk heterojunction, sandwiched between metallic semitransparent contacts, exhibiting 1.24 mA cm^{-2} at 0 V vs RHE and very positive onset potential (OP) at 0.85 V vs RHE using a Pt electrocatalyst. However, the role of light-absorber in this device is covered by the quantum-confined, 2.1 eV band gap energy CdSe NP with the P3HT polymer (dispersed 10:1 against CdSe NP in the blend) involved mainly in charge transport. Even higher performances were reached by Bourgeteau et al. [18] using an architecture integrating P3HT:PCBM bulk heterojunction, selective contacts and, notably, a non-precious MoS_3 co-catalyst. Such photocathode exhibited 8 mA cm^{-2} at 0 V vs RHE and OP as high as 0.6 V vs RHE. In this case the photocathode was not entirely plunged into the PEC cell, only the MoS_3 surface was put in contact with the electrolyte thanks to a rubber seal on the quartz cell. In addition the thick metallic electron selective contact (100 nm Al plus 40 nm Ti) likely made the photocathode opaque to solar radiation hindering the possibility to exploit this configuration for tandem devices in full water splitting systems. Both systems exhibited photocurrent dynamic with photocathodes active for periods of several hours and exhibiting optimum performances for periods of several minutes.

In this work, we demonstrate an efficient hybrid organic-inorganic photocathode based on a P3HT:PCBM bulk heterojunction and transparent selective layers, capable of reaching photocurrent densities above 3 mA cm^{-2} at 0.0 V vs reversible hydrogen electrode (RHE) and an onset potential as high as +0.67 V vs RHE. The optimized photocathode's architecture comprises inorganic charge selective layers (CSL) and hydrogen evolution catalyst. We found that the organic component of the device to retain its light absorption and structural properties in the aqueous system following extended photocathode operation, while photocurrent dynamic is found to result from CSL chemical modification under electrochemical operation. Our findings establish conjugated polymers as a promising class of materials for photoelectrochemical applications and suggest paths for future developments, disclosing new strategies for sustainable H_2 production.

Experimental

Fabrication details.

Photocathodes were fabricated on FTO coated soda-lime glass substrates (Dysol, sheet resistance 15 Ω sq^{-1}) cleaned according to the following protocols: two series of sequential sonication baths in acetone, isopropanol and DI water each lasting for 20 minutes, thermal annealing in a muffle furnace operated in air at 500 °C for 2 hours and plasma cleaning in an inductively coupled reactor for 20 minutes (100 W RF power, excitation frequency 13.56 MHz, 40 Pa of O_2 gas process pressure, background gas pressure 0.2 Pa). Unless specifically mentioned, photocathodes were fabricated according to the architecture FTO/MoO_3/BHJ/TiO_2/Pt. Complementary architectures without hole or electron selective or catalyst layers were also fabricated and specifically referred to when mentioned in the discussion section. The organic polymers absorber film used in every architecture was composed by the semiconducting polymer Poly(3-hexylthiophene-2,5-diyl) as donor and the fullerene derivative [6,6]-Phenyl C61 butyric acid methyl ester as acceptor (P3HT:PCBM blend as follows). P3HT regioregular electronic grade Mn 15000 - 45000 was purchased from Sigma-Aldrich. PCBM 99.5% purity was purchased from Nano C. Both were dissolved in chlorobenzene ACS grade at 1:1 wt. ratio and 25 mg mL^{-1} on a polymer basis. Polymer blend solution was stirred at ambient temperature for 6 hours before use. Polymer thin films were spin casted by means of a Laurell Tech. Corp. spin coater using the following set of parameters: two steps spinning protocol with rotation speeds of 800 rpm for 3 s followed by 1600 rpm for 60 s, respectively, for both sections set accelerations were 34680 rpm s^{-1}, total drop-casted solution volume was 100 µL for each sample. This spin casting protocol produces an P3HT:PCBM blend layer 200 ± 20 nm thick, as measured by means of an Alpha-Step IQ surface profiler. Post thermal annealing in N_2 atmosphere was performed at 130°C for 10 minutes for every device after photoelectrodes fabrication was completed. Pulsed-DC magnetron sputtering source with adjustable repetition frequency and duty cycle was used for Mo and Pt deposition (targets purity 99.99%, purchased from Mateck Gmbh). The vacuum chamber was evacuated to a base vacuum pressure lower than 3.0×10^{-3} Pa before each deposition. For Mo deposition discharge operating pressure was 1 Pa and Argon gas flow 110 sccm, target-substrate distance was fixed at 50 mm. After deposition Mo metal films were thermally treated in a muffle furnace operated in air at 500°C for 30 minutes in order to obtain alpha-phase orthorhombic MoO_3

films exhibiting layered structure. For Pt deposition discharge operating pressure was 15 Pa and Argon gas flow 410 sccm, target-substrate distance was fixed at 80 mm. Fabrication of TiO_2 films by means of pulsed laser deposition was carried out using a TiO_2 target (Testbourne, 99,99% purity) in an Ar/H_2 atmosphere (H_2 content 3,1 % mol) at a total pressure of 15 Pa. Pulsed excimer laser (Coherent KrF, λ = 248 nm) was set at a pulse repetition rate of 20 Hz with 400 mJ energy per pulse and a fluence of 2.5 J cm^{-2}

Materials characterization.

Micrographs of deposited films were acquired by a Zeiss SUPRA40 field-emission scanning electron microscope (SEM) using an operating voltage of 5 kV and a working distance of 2 mm. Structural information is obtained through X-ray diffraction (Philips X'Pert, Cu Ka radiation, Hanawalt phase identification method on PDF-2 dataset) used in reflection mode, measurement parameters were: exposure time: 0.1 s; angular step size: 0.016°. Chemical state information is obtained usig an AXIS Ultra DLDinstrument (Kratos) equipped with an AlKaX-ray source (1486.6 eV) operated at 10 mA, 15 kV. The optical properties of the samples in the range 250-2500 nm are measured with a UV/Vis/nIR spectrometer (Perkin Elmer Lambda 1050) operating with a 150 mm integrating sphere. Work function data were obtained by using a Kelvin Probe Microscope (Bruker, Dimension Icon) in air and at room temperature. A reference sample of graphite (HOPG, highly ordered pyrolytic graphite) was used for calibration, as its work function value (4.6 eV) is well determined.

Raman spectra were recorded by using a visible (VIS) diode laser, emitting at 532 nm, included in a commercial Renishaw InVia Raman microscope in a back scattering configuration, including a monochromator and notch filters system.. Samples were placed on the stage of a Leica microscope, equipped with 50× and 100× short and long working distance objectives. In all measurements, laser power intensity on the sample was kept at values lower than 0.03 mW to avoid laser- induced sample degradation.

Electrochemical characterization.

Photoelectrochemical measurements were carried out in a quartz cell with a three-electrode configuration using an Autolab PGSTAT302N potentiostat/galvanostat. A Pt wire was used as counter electrode (CE) and an Ag/AgCl electrode filled with saturated KCl solution (0.197 V versus the standard hydrogen electrode at 25°C) was used as reference electrode (RE). All the characterizations have been performed by employing 50 mL 0.1M H_2SO_4 (Sigma-Aldrich, 99.999% purity) electrolyte corrected with 0.1M Na_2SO_4 (Sigma-Aldrich, purity 99%) to stabilize the solution at pH 1.37. A 300 W Xe light source equipped with AM filters (Lot Quantum Design, model LS0306) calibrated to 1 sun at the electrode surface in the electrolyte, was used to illuminate the photocathode from the conductive glass side. N_2 gas was bubbled in the electrochemical cell for at least 1 hour before starting each experiment and a constant nitrogen flow was maintained during the whole measurement to completely remove the molecular oxygen contained in the electrolytic solution. Linear sweep voltammetry technique has been employed to evaluate the response of photocathodes under dark and illumination conditions by alternatively chopping the light source. Scan rate used in every voltammetry measurement was 10 mV sec^{-1}. LSV measurement outputs were found to be sensitive to the sample's history; LSV data shown in the main text were recorded after sample's polarization at + 0.18 V vs RHE in potentiostatic conditions using the electrolytic solution described above, when the photocurrent signal reached the maximum value and the device exhibited several minutes of stable behaviour. Samples' time stability has been monitored by chronomperometric tests for 150 minutes using always the same electrolyte described above. Ions intercalation (H^+ and Na^+) into the layered α-MoO3 and formation of molybdenum bronzes was observed both by polarizing the electrode at +0.18V vs RHE under potentiostatic conditions (chronoamperometry experiments) as well as during LSV measurements when the potential was swept at voltages lower than 0.48V vs RHE.

Incident photon-to-electron conversion efficiency (IPCE) measurements were performed under light emitted from a 300 W Xe lamp (Cermax PE 300 BUV) passed through a monochromator (Bausch & Lomb, bandwidth 10 nm FWHM). The photocathode was fixed inside a test cell with quartz window and illuminated from the glass substrate side. In three-electrode configuration the system's photocurrent response was measured at each wavelength while holding the potential constant at + 0.18 V vs RHE. This photoresponse was compared against that of a calibrated Si photodiode to determine the IPCE at each wavelength.

For analysis of evolved gas products, the photocathode was fixed inside a gastight test cell, immersed in 15 mL of pH 1.37 electrolyte, and illuminated from the glass substrate side by light from a 450 W Xe lamp (Osram, ozone-free) equipped with an AM1.5G filter (Lot QD) calibrated to one sun intensity. Rapid stirring was applied, and a 19.99 sccm (+/− 0.5%, controlled by a mass flow controller, Bronkhorst EL-Flow) flow of Ar was continuously bubbled through the cell with the outflow periodically injected into a gas chromatograph (TRACE Ultra with PDD detector, Thermo Scientific; ShinCarbon ST column, Restek) for in-line characterization of evolved hydrogen. The GC response was calibrated using a certified standard for hydrogen (Carbagas). For photocathode testing a three-electrode configuration was used, with a Ag/AgCl (sat. KCl) reference electrode and a Pt wire counter electrode (held behind a porous ceramic diaphragm to minimize the product crossover), and the photocurrent and hydrogen content of the carrier gas outflow were measured simultaneously during extended potentiostatic operation. The expected H_2 ppm values were calculated from the photocurrent and carrier gas flow rate, accounting for the volume-dependent accumulation of evolved gas in the cell.

Results and discussion

Hybrid organic-inorganic photocathodes architecture

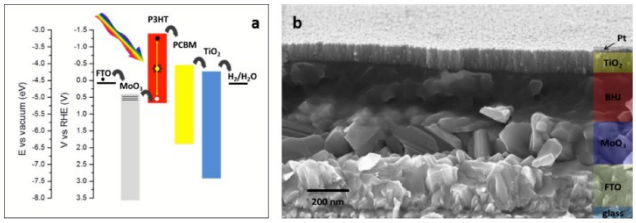

Figure 1: Structure of the hybrid photocathode. **a.** Overview of the energy band edge positions for the semiconductors of the hybrid photocathode and redox level of the water reduction reaction, the direction of the arrows indicating electrons injection at interfaces. The black lines within the MoO_3 energy band indicate energy levels originating from the protonation of MoO_3 film. **b.** High resolution scanning electron micrograph cross sectional image of the different layers composing the photocathode architecture. From bottom to top: FTO transparent conductive oxide, hole blocking α-MoO_3 layer, P3HT:PCBM bulk heterojunction, electron selective TiO_2 layer and Pt electrocatalyst layer.

A critical feature in designing a water splitting photoelectrodes is the device's built-in potential gradient allowing electrons and holes to be separated and driven toward the catalytic sites for their respective half-reactions (Figure 1a). The same applies in organic photovoltaics (OPV) employing a BHJ, where charge-selective layers are essential for proper charge extraction at the contacts. [19] A challenge to this approach is that most of the materials used in OPV as hole-selective (HSL) or electron-selective layers (ESL) are either water soluble (amorphous MoO_3 and V_2O_5, LiF, Ca), prone to dissolution in acidic environment (ZnO, Al), or electrochemically unstable due to ion penetration and doping phenomena (PEDOT:PSS). [20] Moreover, the ESL conduction band must be not only positive with respect the acceptor LUMO for efficient electron extraction from the BHJ, but also negative of the water reduction potential and stable towards reductive degradation reactions at potentials within the bandgap. TiO_2 is an ideal candidate to fulfil these requirements and has been demonstrated both as ESL in OPVs [19] and as electron-conducting overlayer in photocathodes for water splitting. [21,22] An HSL is necessary to harvest holes while repelling electrons, thereby reducing recombination processes at the interface and consequently enhancing carriers' quasi-Fermi energies splitting in order to maximize photovoltage. Recently, amorphous molybdenum oxide has emerged as a promising HSL for high-efficiency OPVs. [23] MoO_3 is n-type in nature, and its apparent hole-selectivity is the result of the formation of a highly p-type doped interface with conjugated polymers having ionization energies (IE) lower than the oxide work function (WF). [24, 25] Its large band gap (3.0 eV) and high transmittance enables illumination through the HSL layer. In its α form MoO3 exhibits a layered orthorhombic crystal structure with two MoO_6 octahedron nets layers linked by Van der Waals forces along the [0 1 0] direction. [26, 27] Recently, it gained attention as an alternative 2D semiconductor in the form of single bi-layer (i.e. the two connected MoO_6 octahedral planes) for several applications. [28] In particular, high electron mobility (up to 1000 $cm^2\ V^{-1}\ s^{-1}$) has been demonstrated for a field-effect transistor based on reduced α-MoO_3 nanosheets. [26, 29] An unavoidable consequence of the intrinsic α-MoO_3 large bandgap is its extremely low carrier concentration that makes it impossible to achieve good electron injection. Thereafter, careful defect engineering into intercalated/reduced forms of α-MoO_3 allowed the authors to reach good conductivities by enhancing electron concentration while retaining the high mobility of the 2D semiconductor. α In light of the use in water it has to be considered that amorphous MoO_3 is highly soluble in water, while α-MoO_3 is not.

Hence, we developed a H_2 evolution device architecture (Figure 1b) in which the photoactive P3HT:PCBM bulk heterojunction is sandwiched between low solubility charge selective layers: crystalline α-MoO_3 as hole-selective layer and amorphous TiO_2 as electron-selective layer and catalyst support. The stack was constructed as a photocathode in which the ESL routes the photogenerated electrons towards the Pt electrocatalyst where they reduce aqueous protons and evolve H_2. The α-MoO_3 was obtained by Mo sputter-deposition onto F:SnO_2 (FTO) followed by thermal oxidation. A P3HT:PCBM blend was subsequently spin-coated to form the BHJ layer. Amorphous titanium oxide was deposited on top of the polymeric blend by pulsed layer deposition (PLD) due to its capability of depositing oxide layers on polymeric semiconductors while preserving their functionalities [31] and providing good control of nanostructure and stoichiometry. [32] Finally, Pt catalyst was sputter-deposited onto the TiO_2 top surface as catalyst for the hydrogen evolution reaction (HER). Additional fabrication details can be found in the experimental section

Photoelectrochemical characterization

The photoelectrochemical responses of the optimized photocathode and several architectural variations are shown in Figure 2a.

Throughout this work (unless otherwise specified) a 0.1M H_2SO_4-Na_2SO_4 solution buffered at pH 1.37 was used as electrolyte, illumination was provided by a calibrated AM1.5 solar simulator at 1 sun intensity, and the onset potential (OP) is defined as the potential at which a photocurrent density of 10 μA cm^{-2} is reached. Under illumination, the simple

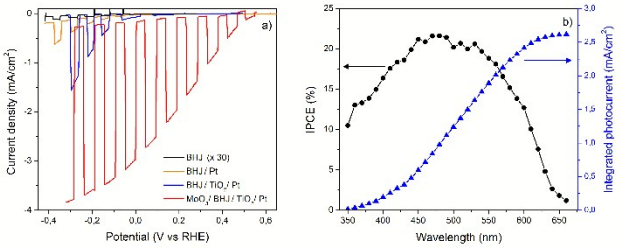

Figure 2: Photoelectrochemical device characterization. **a.** Current–potential characteristics measured in 0.1 M H_2SO_4-Na_2SO_4 solution at pH 1.37, under chopped AM 1.5 light illumination (100 W cm^{-2}) for different hybrid organic/inorganic photocathodes architectures: (black curve) FTO/P3HT:PCBM with total current density multiplied 30 times in the plot scale, (orange curve) FTO/P3HT:PCBM/Pt, including an electrocatalytic layer, (blue curve) FTO/BHJ/TiO_2/Pt including both electron selective/catalysit support and electrocatalytic layers and (red curve) FTO/MoO_3/BHJ/TiO_2/Pt a complete architecture including also the hole blocking layer. **b.** Incident photon-to-current conversion efficiency (IPCE) of the FTO/MoO_3/BHJ/TiO_2/Pt photocathode was determined after initial activation under white light at constant bias +0.1 V vs RHE. Integration of the IPCE response over the AM1.5G spectral flux is also depicted.

architecture without HSL, ESL and electrocatalyst (FTO/BHJ) shows a maximum net photocurrent of only 2.5 μA cm^{-2} at -0.3 V vs RHE and less than 0.5 μA when evaluated in potentiostatic mode at positive voltages vs RHE (see figure S1). In this basic semiconductor-liquid junction the organic component is found to preserve its light absorption and structural properties after potentiostatic operation (see figures S2 and S3a). By adding a Pt layer, choosing low energy deposition conditions, [33] the performances of the photocathode markedly improved exhibiting an OP at 0.0 V vs RHE and a maximum net current around 400 μA cm^{-2} at -0.3 V vs RHE, also in this case the structural properties of the semiconducting polymer as measured by Raman spectroscopy are found unchanged after prolonged potentiostatic operation (see figure S3b). In this case the presence of the catalysts allowed operating the system in chronoamperometric mode at much higher current levels (several hundreds of μA cm^{-2}) providing a more significant environment for organic materials stability. Addition of a TiO_2/Pt layer on the surface of the BHJ enhanced the photocurrent response, yielding more than 1 mA cm^{-2} at -0.3 V vs RHE with a positive OP of +0.2 V vs RHE. Here we note that the TiO_2 layer covers exclusively the roles of ESL and catalyst support and not a protective role, in fact its porous nature allows permeation of the electrolyte towards the lower layers of the photocathode structure (see figure S4). The most significant improvement in performance was found upon incorporation of the MoO_3 layer. Within their stability window, the optimized architecture exhibited an OP of +0.55 V vs RHE, and photocurrent densities of 3 mA cm^{-2} at 0.0 V vs RHE and 2.5 mA cm^{-2} at +0.18 V vs RHE. These figures are placed among the best performances reported for a photoelectrochemical device architecture based on organic absorber materials, where only a few reports describe photocathodes significantly exceeding 1 mA cm^{-2} net photocurrent at positive bias. [17,18]

The photovoltage generated by the hybrid organic-inorganic photocathode is comparable to the open circuit voltages of the best photovoltaic cells,[30] as well as organic photocathodes [18] based on a P3HT:PCBM BHJ and competitive with inorganic photocathodes based on Cu_2O or Si. [22,34] It is important to emphasize that for our photocathodes employing MoO_3 as HSL, the reported photocurrent density vs potential (J–V) data are not representing the initial behavior (at t = 0 s) of the device when measured in the three electrodes cell but they were measured after 20 minutes of operation in chronoamperometric mode. The J–V curves therefore represent the "peak" performance achieved for a chosen configuration (e.g. layers thickness) of the optimized architecture. Similarly, the IPCE (Figure 2b) for the FTO/MoO_3/BHJ/TiO_2/Pt architecture was measured after 20 minutes of operation in chronoamperometric mode. The electrode showed a photoresponse in the range from 350 to 650 nm, consistent with what is expected from the P3HT:PCBM BHJ, and a maximum IPCE of about 22% between 450 and 550 nm. Integration of the IPCE over the AM1.5G spectrum predicts a one-sun photocurrent of approximately 2.6 mA cm^{-2}, correlating well with the photocurrent measured at the same bias potential under simulated sunlight.

In order to further prove the photoelectrochemical response and H_2 production by the hybrid photocathode, hydrogen quantification measurements were performed. The evolution of hydrogen was measured by in-line gas chromatography during chronoamperometric (CA) operation under simulated sunlight illumination, as shown in Figure 3a.

Despite the evolving current density over time, the amount of measured hydrogen correlated extremely well with the hydrogen expected from the photocurrent magnitude over time, yielding near-unity Faradaic efficiencies during the device operation. This confirms that the observed photocurrents

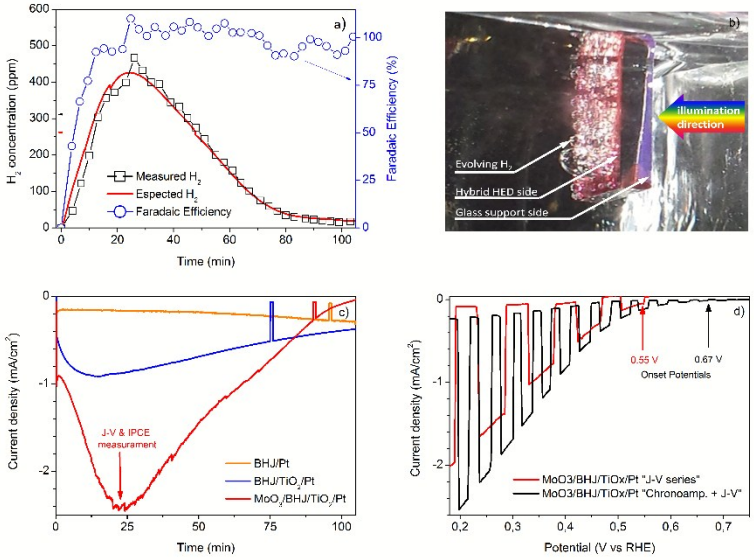

Figure 3: Product analysis and examination of device behaviours. **a.** H_2 evolution monitored by gas chromatography during continuous photocathode operation under simulated sunlight (AM1.5, 100 W cm^{-2}) in electrolyte solution (0.1 M H_2SO_4-Na_2SO_4 at pH 1.37). Left y-axis refers to periodic measurements of the hydrogen content of the carrier gas (black squares) and the expected hydrogen content, derived from the measured photocurrent in potentiostatic operation (red line). Faradaic efficiency, calculated as the ratio between the measured and the expected hydrogen content, is shown as the blue circles. Illumination and electrolyte conditions are identical through all panels in this figure. **b.** Photograph of the hybrid organic/inorganic photocathode evolving hydrogen during potentiostatic operation. **c.** Photocurrent density in potentiostatic operation for the full hybrid photoelectrode (red line, CA measured at + 0.18 V vs RHE) and two complementary architectures, lacking HSL (blue line, CA

indeed corresponded to the reduction of water to hydrogen, rather than to non-Faradaic corrosion processes. Only during the rising part of the chronoamperogram does the measured H_2 fall below the concentration predicted by the photocurrent density, a phenomenon which, along with the dynamic behavior of the CA, can be related to reduction of the MoO_3 HSL, as discussed later. Nevertheless, hydrogen is produced at high yield throughout, validating the device performance as an H_2-evolving photocathode. The device under operation in the three-electrode cell, with visible bubbles of hydrogen evolving from the surface, is depicted in Figure 3b.

Different photocurrent dynamics (Figure 3c) were observed for selected architectures under fixed illumination and bias. The CA of the FTO/BHJ/Pt and FTO/BHJ/TiO_2/Pt architectures demonstrate operational activity over more than two hours. This is markedly different from photocurrent time-evolution observed for complete architectures including MoO_3 HSL. As shown above, addition of the MoO_3 hole selective layer dramatically improved the OP and photocurrent by reducing recombination losses at the contacts.[24,35] However, this peak performance only emerges after device biased operation in the electrolyte (around 20 minutes when polarized at +0.18 V vs RHE). After peaking the FTO/MoO_3/BHJ/TiO_2/Pt architecture shows around 10 minutes of stable operation followed by a nearly-linear photocurrent decline over more than 90 minutes, which is not a result of device's structure mechanical failure (see Figure S6). Moreover, it was found that OPs depend on the photocathode's polarization history. Compared to the most positive OPs measured when repeating a series of J-V scans (OP = +0.55 V vs RHE, sweeping between +0.8 and +0.18 V vs RHE), a significantly higher OP of +0.67 V vs RHE was obtained when the J-V curve was measured after a CA (+0.18 V vs RHE, AM1.5) until the point of maximum photocurrent point (Figure 3d). The latter method was used also before acquiring the IPCE spectrum.

Analysis of photocathode component influence on electrochemical performances

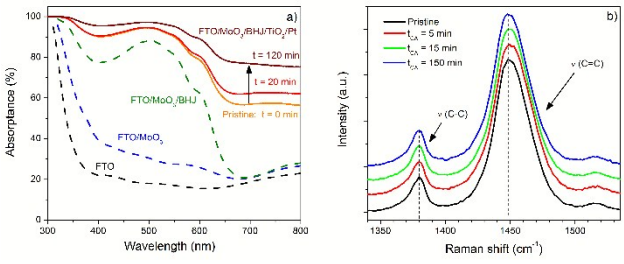

Figure 4: Spectroscopic analysis of device and components. **a** UV-Vis-nIR absorptance spectra of different architectures before and after CA operation. FTO coated glass substrate (black dashed line) and FTO/α-MoO_3 (blue dashed line) are plotted as reference. The absorptance of the FTO/α-MoO_3/BHJ architecture (green dashed lines) is measured before CA experiments. FTO/α-MoO_3/BHJ/TiO_2/Pt architecture spectra are shown before CA (solid orange line), after 20 minutes (red solid line) and after 120 min (dark red solid line) of operation; **b.** Resonant Raman absorption spectra of FTO/α-MoO_3/BHJ/TiO_2/Pt photocathodes are measured before CA (black line), after 5 minutes (red line), 15 minutes (green line) and 150 minutes (blue line) of operation. The graph shows a zoom over the spectral range 1350−1550 cm^{-1}, sensitive to π-electron delocalization of the rr-P3HT chain (peaks at 1449 cm^{-1}, assigned to rr-P3HT thiophene ring stretch/shrink vibrational mode, and at 1380 cm^{-1}, assigned to intra-ring thiophene stretch vibrational mode). Dashed lines indicate peaks centre positions.

We therefore set out to identify and understand the source of the behavior reported above by performing in-depth study of each layer composing the device. We first focused on investigating possible irreversible degradation of the BHJ. We carried out UV-Vis and resonant Raman spectroscopy measurements on FTO/MoO_3/BHJ/TiO_2/Pt photocathodes before and after prolonged CA operation, finding consistent results. UV-Vis absorption (Figure 4a) shows no noticeable change in the spectral shape after 2 hours of operation in chronoamperometric mode. Even though the absorptance of the FTO/MoO_3/BHJ/TiO_2/Pt architecture increases after CA due to MoO_3 intercalation with H+ cations (see Figure 5a and following discussion), the 600 nm spectral feature related to long range order of rr-P3HT crystalline structure is unchanged with time. The rr-P3HT absorption spectral shape between 400 and 650 nm did not change significantly, meaning that irreversible processes, associated with a polymer conjugation loss, are negligible. [36] In performing resonant Raman absorption measurements (Figure 3b) on the same samples we focused on the spectral region known to be sensitive to π-electron delocalization (1350 cm-1 – 1550 cm-1).[37] In agreement with previous results obtained for rr-P3HT thin films exposed to both light and aqueous electrolyte but supporting substantially lower current densities,[12] we did not observe significant changes in the position of the two main peaks at 1378 cm^{-1} and at 1445 cm^{-1} (assigned to C−C stretching and in-phase C=C/C−C stretching/shrinking of the aromatic thiophene ring, respectively), nor in their intensity ratio in the Raman spectra of FTO/MoO_3/BHJ/TiO_2/Pt photocathodes after different CA times (see Figure S5) This analysis allowed us to safely exclude the occurrence of significant structural variation (e.g., change in the conjugation length) caused by the polymer/environment interactions and surmise that the photocurrent dynamics is not a result of polymers blend structure modifications but rather from some other component of the photocathode architecture.

The stability of the organic semiconductors is further confirmed by the net photocurrent generated by the FTO/BHJ/Pt architecture even after 2.5 hours of continuous operation (Figure 3b). Hence, we can assert that the organic semiconductors are stable in water and that can produce hydrogen over extended periods of time. Architectures incorporating a TiO_2 ESL showed improved OP (Figure 2a) resulting from the charge-selective behavior of the interface, yet FTO/BHJ/TiO_2/Pt photocathodes exhibited a gradually decreasing photocurrent response under extended CA (Figure 3b). This decrease is likely the result of changes in TiO_2 induced by its operation in acidic solution at potentials negative of RHE. Under these conditions, TiO_2 is prone to the reductive formation of Ti^{3+} states acting as act to traps for photogenerated charges [21, 38], possibly reducing the charge selective ability of the junction and inhibiting the charge injection into the surface catalyst. Despite the known risk of TiO_2 instability as evident in its Pourbaix diagram[39], we were constrained to operate in acidic electrolyte by the pH-V stability window of the HSL component, as described below. Nevertheless, this slight decay attributable to TiO_2 cannot fully

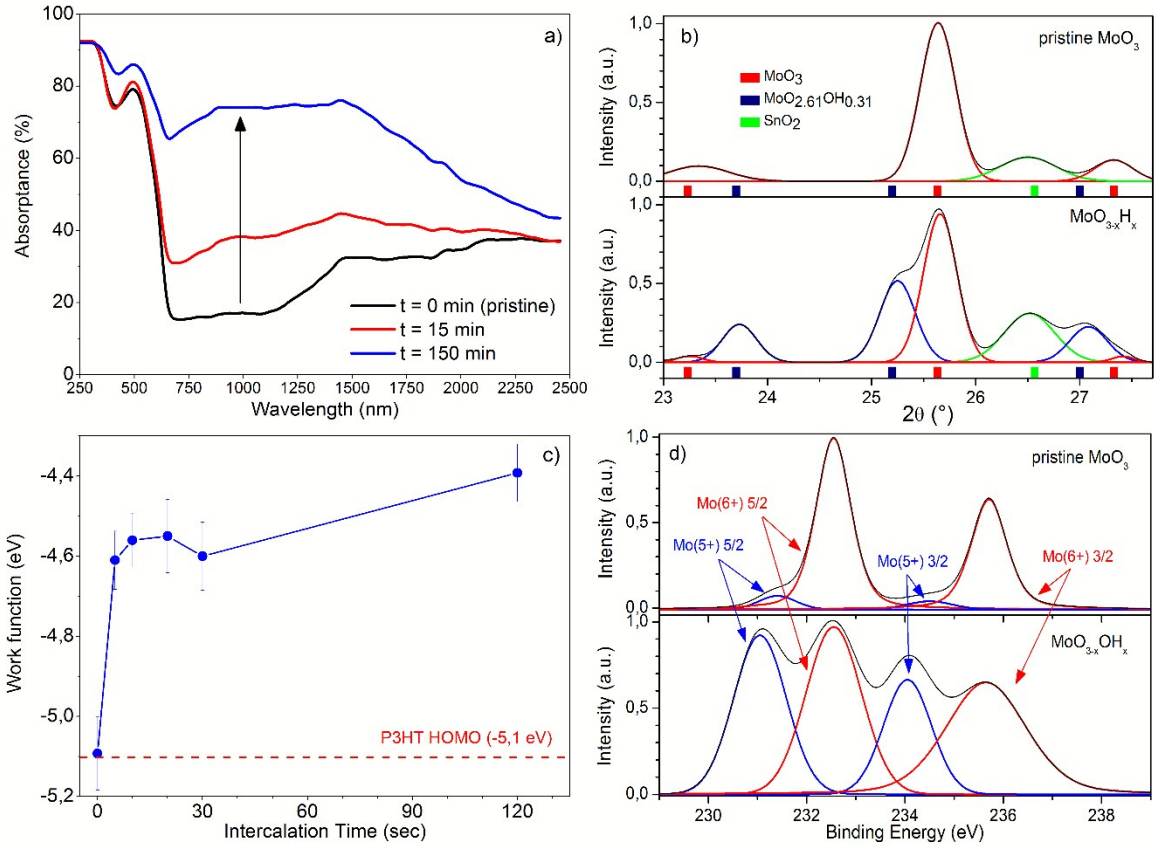

Figure 5: Evolution of MoO_3 properties. a, UV-Vis-nIR absorptance spectra of FTO/α-MoO_3/BHJ/TiO_2/Pt photocathodes before (black line), after 15 minutes (red line) and after 150 minutes (blue line) of CA at pH 1.37 and +0,18 V vs RHE. Pristine photocathodes reference spectrum shows the α-MoO_3 UV cut-off around 375 nm (E_g = 3.3 eV), the rr-P3HT absorption band around 400-600 nm and the IR plasmonic absorption if the FTO layer above 1250 nm. Samples absorptance measured after CA exhibit a pronounced peak arising around 1000 nm, which is interpreted as the plasmonic absorption of the $MoO_{3-x}OH_x$ layer (black arrow); **b**, Mo 3d x-ray photoemission spectra of FTO/α-MoO_3 films as-deposited (**top**) and after (**bottom**) electrochemical (EC) intercalation. The formation of reduced 5+ states after intercalation is readily observed in the spectra after a few seconds of films polarization; **c**, EC intercalated FTO/MoO_3 films ($MoO_{3-x}OH_x$) work function as measured by Kelvin probe plotted against intercalation time. As reference, a typical literature HOMO energy level for rr-P3HT (red dashed lines) is shown; **d**, XRD patterns for α-MoO_3 films before (**top**) and after (**bottom**) EC intercalation. Backgrounds were subtracted from the measured patterns. Literature reflections of MoO_3 molybdite (red), hydroxy-molybdenum oxide (blue) compound and SnO_2 cassiterite (green, arising from the substrate glass) are shown below the patterns for comparison.

explain the dynamic behavior of the complete photocathode architecture.

In order to understand the dynamic behavior of the FTO/MoO_3/BHJ/TiO_2/Pt device it is important to consider that the electrolyte interacts with each layer of the photocathode. After fabrication, sparse µm-size fissures were routinely observed (see Figure S7) on the TiO_2 over-layer, exposing the underlying BHJ. This was a consequence of the polymers blend film volume variation during the final annealing step that is necessary for the formation of an efficient BHJ and proper contact between the blend and the selective contacts. Hence, the photocathode may be considered as a porous structure where the electrolyte permeates and interacts with each layer. In fact, chronoamperograms at different operating potentials (Figure S8) show that the maximum peak current is obtained after 20 minutes of polarization at about +0.18 V vs RHE, whereas more negative operating potentials lead to similar but more rapid photocathode dynamics. On the contrary, potentials close to +0.4 V vs RHE leads to a more stable operation, with photocurrent persisting for more than 2 hours. Optical absorption spectra taken at different points of the chronoamperogram for a FTO/MoO_3/BHJ/TiO_2/Pt photocathode with a reduced Pt loading (in order to avoid parasitic absorption by the metal), Figure 5a, clearly show a significant plasmonic absorption band in the near infrared region suggesting a large carrier density build up. Indeed, we observe an increasing blue coloration of the HSL during CA operation. As shown in Figure 5b, XPS analysis confirms the formation of these reduced Mo(5+) states in high percentage, also in correlation with a MoO_3-xOH_x phase observed by XRD (Figure 5d). These results are in accordance to several earlier studies. [30, 39, 40] A deleterious effect of the intercalation process is the decrease of the MoO_3 HSL work function (Figure 5c and figure S9) as proven by Kelvin probe measurements. We therefore hypothesize that during operation, light cations (H^+ and Na^+) intercalate into the α-MoO_3 layers resulting in a high density of shallow gap states near the Fermi level. [30] The consequent increase in conductivity of the HSL favors electron

injection from the FTO to the photogenerated hole in the rr-P3HT, with a positive impact on the photocurrent and fill factor of the photocathode. Unfortunately, the intercalation process for potentials negative of +0.4 V vs RHE is not a self-limiting process, causing the α-MoO_3 layer to be reduced to sub-stoichiometric phases (MoO_3-xOH_x, MoO_2) likely through an H_2 insertion / H_2O abstraction mechanism. Reduced molybdenum oxide compounds exhibit decreased work functions (Figure 5c) which disrupt the favorable energy levels alignment at the oxide/organic interface (i.e. requiring $WF_{MoO3} > IE_{P3HT}$) [41] thus compromising the selectivity of the contact and progressively reducing the photocathode's OP (see Figure S10). The trade-off between α-MoO3 intercalation and reduction processes dictates the photocathode's photocurrent temporal evolution during CA (see Figure 3b and Figure S11).

These results demonstrate the importance of materials compatibility when operating in aqueous electrochemical environments. The H_2 evolution device clearly undergoes significant changes in structure and performance over extended operation. Interestingly, our data showed that the performances decay cannot be addressed to the organic polymers blend component, which did not show significant alterations while operating in the electrolyte, but rather the metal oxide charge-selective layer that produce dynamic behaviors. An improved TiO_2 ESL could be made compact and defect-free in order to protect the underlying materials, namely the MoO_3 HSL, from exposure to the aqueous electrolyte. Previous studies have shown that atomic layer deposition (ALD) of TiO_2 is a promising route toward stabilizing inorganic semiconductors as photocathodes and photoanodes, [21,22] but very few reports have accomplished successful oxide ALD onto polymer films. We are presently exploring this approach toward a more protective ESL. Nevertheless, the partially reduced forms of MoO_3 clearly show favorable electronic and interface properties as an HSL component in this architecture, so care must be taken in targeting the ideal phase during the synthetic steps, followed by proper isolation of the HSL component from water to avoid undesired MoO_3 reduction. Examination of the Pourbaix diagram of Mo oxides [39] reveals a small region of MoO_3 stability in the pH–V space, limiting the pH range up to 1.4 and to quite positive potentials, higher than +0.4 V vs RHE. While this voltage range might be viewed as a limitation for this architecture, it is important to remember that a major goal for hydrogen-evolving photocathodes is to operate at potentials as positive as possible in order to efficiently work in a tandem configuration with a photoanode or a PV cell. [3] From this perspective we note (see Figure 5a) that 80% nIR average transmittance (800 – 1200 nm) for the uncatalyzed (R ≈ 5%), as-deposited photocathode stack (fully transparent MoO_3 HSL) and 60% for the uncatalyzed device exhibiting best performances after polarization (intercalated MoO_3-xOH_x HSL), are possible with this architecture but in the current realization an optimization of the Pt layer thickness is required in order to reduce the device's overall front surface reflectivity. As an alternative route towards improved stability, the HSL material could be exchanged for a more water-stable candidate, but this will prove to be a challenge since many of the well-studied HSL materials (ITO, PEDOT, amorphous MoO_3, NiO, V_2O_5) are known or predicted to be unstable under reductive electrochemical conditions, a common trait among large work function metal oxides.

Conclusions

We demonstrated the potential of organic semiconductors as active materials in a photocathode for aqueous H_2 production with a maximum photocurrent above -3 mA cm^{-2} at 0 V vs RHE and an onset potential as high as +0.67 V vs RHE, competitive with the state-of-the-art reported photocathodes. To the extent of our knowledge these values are among the few reported photoelectrochemical device architectures employing conjugated polymers as active materials exceeding 1 mA cm^{-2} generated photocurrent at positive potential vs RHE. A Faradaic efficiency of 100% for water reduction and operation up to 2 hours were demonstrated. Most important, for this new class of systems, is the demonstration that organic semiconductors are per se suitable for stable and efficient hydrogen evolution applications. The study further examined the importance of proper choice of selective contacts, taking into account the harsh environment of water splitting experiments. We anticipate that with new and more compatible HSL and ESL components, stable operation at photocurrents close to the maximum achievable with OPV, on the order of 10 mA cm^{-2} at positive bias, are achievable. Moreover, one can explore the rich library of organic semiconductors developed for OPVs in order to realize large area, solution processed multijunction configurations [42] with optimized photoanodes and photocathodes for renewable and low cost direct conversion of solar energy into hydrogen.

Acknowledgements

The work was supported by EU through the Future and Emerging Technologies (FET) programme under the FP7, Collaborative Project 309223 (PHOCS, Photogenerated Hydrogen by Organic Catalytic Systems).

Author contributions statement: F.F., in collaboration with A.G. and G.T., fabricated the devices and performed optical and Raman analysis, S.B., in collaboration with S.L. and H.C. performed the electrochemical characterization. M.S. and M.T.M. carried out the GC and IPCE measurements. L.M. performed XPS measurements, G.M. performed XRD measurements, and A.S. performed Kelvin probe measurements. F.D.F. and M.R.A. supervised the work. All authors discussed the results, interpretations and contributed to the manuscript drafting.

References

1 a) N. S. Lewis, D. G. Nocera, *Proc. Natl. Acad. Sci*. 2006, **103**, 15729; b) Y. Tachibana, L. Vayssieres, J. R. Durrant, *Nat Photon* 2012, **6**, 511

2 M. G. Walter, E. L. Warren, J. R. McKone, S. W. Boettcher, Q. Mi, E. A. Santori, N. S. Lewis, *Chem. Rev*. 2010, **110**, 6446
3 M. S. Prévot, K. Sivula, *J. Phys. Chem. C* 2013, **117**, 17879
4 S. Hu, C. Xiang, S. Haussener, A. D. Berger, N. S. Lewis, *Energy Environ. Sci*. 2013, **6**, 2984
5 a) R. S. Sprick, J.-X. Jiang, B. Bonillo, S. Ren, T. Ratvijitvech, P. Guiglion, M. A. Zwijnenburg, D. J. Adams, A. I. Cooper, *J. Am. Chem. Soc*. 2015, **137**, 3265; b) V. S. Vyas, B. V. Lotsch, *Nature* 2015, **521**, 41
6 A. Facchetti, *Chem. Mater*. 2011, **23**, 733
7 a) F. C. Krebs, *Sol. Energ. Mat. Sol. Cells* 2009, **93**, 394; b) M. Caironi, Y. Y. Noh, *Large area and flexible electronics*, John Wiley and Sons, 2015.
8 a) S. Bellani, A. Ghadirzadeh, L. Meda, A. Savoini, A. Tacca, G. Marra, R. Meira, J. Morgado, F. Di Fonzo, M. R. Antognazza, *Adv. Funct. Mater*. 2015, **25**, 4531; b) O. Winther-Jensen, B. Winther-Jensen, D. R. MacFarlane, *Electrochem. Commun*. 2011, **13**, 307; c) H. Yan, Y. Huang, *Chem. Commun*. 2011, **47**, 4168
9 a) G. Suppes, E. Ballard, S. Holdcroft, *Polym. Chem*. 2013, **4**, 5345; b) B. Winther-Jensen, K. Fraser, C. Ong, M. Forsyth, D. R. MacFarlane, *Adv. Mater*. 2010, **22**, 1727
10 H. J. Park, J. Y. Lee, T. Lee, L. J. Guo, *Adv. Energy Mater*. 2013, **3**, 1135
11 a) T. Bourgeteau, D. Tondelier, B. Geffroy, R. Brisse, C. Laberty-Robert, S. Campidelli, R. de Bettignies, V. Artero, S. Palacin, B. Jousselme, *Energy Environ. Sci.* 2013, **6**, 2706; b) A. Guerrero, M. Haro, S. Bellani, M. R. Antognazza, L. Meda, S. Gimenez, J. Bisquert, *Energy Environ. Sci*. 2014, **7**, 3666
12 S. Bellani, D. Fazzi, P. Bruno, E. Giussani, E. V. Canesi, G. Lanzani, M. R. Antognazza, *J. Phys. Chem. C* 2014, **118**, 6291
13 M. R. Antognazza, D. Ghezzi, D. Musitelli, M. Garbugli, G. Lanzani, *Appl. Phys. Lett*. 2009, **94**, 243501
14 a) E. Lanzarini, M. R. Antognazza, M. Biso, A. Ansaldo, L. Laudato, P. Bruno, P. Metrangolo, G. Resnati, D. Ricci, G. Lanzani, *J. Phys. Chem. C* 2012, **116**, 10944; b) M. Haro, C. Solis, G. Molina, L. Otero, J. Bisquert, S. Gimenez, A. Guerrero, *J. Phys. Chem. C* 2015, **119**, 6488; c) M. P. Gustafson, N. Clark, B. Winther-Jensen, D. R. MacFarlane, *Electrochim. Acta* 2014, **140**, 309
15 a) S. Licht, B. Wang, S. Mukerji, T. Soga, M. Umeno, H. Tributsch, *J. Phys. Chem. B* 2000, **104**, 8920; b) C. G. Morales-Guio, L. Liardet, M. T. Mayer, S. D. Tilley, M. Grätzel, X. Hu, *Angew. Chem. Int. Ed*. 2015, **54**, 664
16 a) Q. Ding, F. Meng, C. R. English, M. CabÃ¡n-Acevedo, M. J. Shearer, D. Liang, A. S. Daniel, R. J. Hamers, S. Jin, *J. Am. Chem. Soc.* 2014, **136**, 8504; b) M. Moriya, T. Minegishi, H. Kumagai, M. Katayama, J. Kubota, K. Domen, *J. Am. Chem. Soc*. 2013, **135**, 3733
17 L.-H. Lai, W. Gomulya, M. Berghuis, L. Protesescu, R. J. Detz, J. N. H. Reek, M. V. Kovalenko, M. A. Loi, *ACS Appl. Mater. Interfaces* 2015, **7**, 19083
18 T. Bourgeteau, D. Tondelier, B. Geffroy, R. Brisse, R. Cornut, V. Artero, B. Jousselme, *ACS Appl. Mater. Interfaces* 2015, **7**, 16395
19 E. L. Ratcliff, B. Zacher, N. R. Armstrong, *J. Phys. Chem. Lett*. 2011, **2**, 1337
20 E. Stavrinidou, P. Leleux, H. Rajaona, D. Khodagholy, J. Rivnay, M. Lindau, S. Sanaur, G. G. Malliaras, *Adv. Mater*. 2013, **25**, 4488
21 A. Paracchino, N. Mathews, T. Hisatomi, M. Stefik, S. D. Tilley, M. Gratzel, *Energy Environ. Sci*. 2012, **5**, 8673
22 B. Seger, D. S. Tilley, T. Pedersen, P. C. K. Vesborg, O. Hansen, M. Gratzel, I. Chorkendorff, *R. Soc. Chem. Adv.* 2013, **3**, 25902
23 a) Y. Sun, C. J. Takacs, S. R. Cowan, J. H. Seo, X. Gong, A. Roy, A. J. Heeger, *Adv. Mater*. 2011, **23**, 2226; b) L.-M. Chen, Z. Xu, Z. Hong, Y. Yang, *J. Mater. Chem*. 2010, **20**, 2575
24 M. Kröger, S. Hamwi, J. Meyer, T. Riedl, W. Kowalsky, A. Kahn, *Appl. Phys. Lett*. 2009, **95**, 123301
25 a) K. H. Wong, K. Ananthanarayanan, J. Luther, P. Balaya, *J. Phys. Chem. C* 2012, **116**, 16346; b) M. Kröger, S. Hamwi, J. Meyer, T. Riedl, W. Kowalsky, A. Kahn, *Org. Electron*. 2009, **10**, 932
26 S. Balendhran, S. Walia, H. Nili, J. Z. Ou, S. Zhuiykov, R. B. Kaner, S. Sriram, M. Bhaskaran, K. Kalantar-zadeh, *Adv. Funct. Mater*. 2013, **23**, 3952
27 B. Mendoza-Sánchez, T. Brousse, C. Ramirez-Castro, V. Nicolosi, P. S. Grant, *Electrochim. Acta* 2013, **91**, 253
28 T. S. Sian, G. B. Reddy, S. M. Shivaprasad, Jpn. *J. Appl. Phys*. 2004, **43**, 6248
29 M. H. Lee, K. Takei, J. Zhang, R. Kapadia, M. Zheng, Y.-Z. Chen, J. Nah, T. S. Matthews, Y.-L. Chueh, J. W. Ager, A. Javey, *Angew. Chem. Int. Ed*. 2012, **51**, 10760
30 M. Vasilopoulou, A. M. Douvas, D. G. Georgiadou, L. C. Palilis, S. Kennou, L. Sygellou, A. Soultati, I. Kostis, G. Papadimitropoulos, D. Davazoglou, P. Argitis, *J. Am. Chem. Soc*. 2012, **134**, 16178
31 A. Luzio, F. G. Ferré, F. D. Fonzo, M. Caironi, *Adv. Funct. Mater*. 2014, **24**, 1790
32 L. Passoni, L. Criante, F. Fumagalli, F. Scotognella, G. Lanzani, F. Di Fonzo, *ACS Nano* 2014, **8**, 12167
33 F. Fumagalli, J. Martí-Rujas, F. Di Fonzo, *Thin Solid Films* 2014, **569**, 44
34 J. Azevedo, L. Steier, P. Dias, M. Stefik, C. T. Sousa, J. P. Araujo, A. Mendes, M. Graetzel, S. D. Tilley, *Energy Environ. Sci*. 2014**, 7**, 4044
35 N. K. Elumalai, A. Saha, C. Vijila, R. Jose, Z. Jie, S. Ramakrishna, *Phys. Chem. Chem. Phys*. 2013, **15**, 6831
36 M. Manceau, A. Rivaton, J.-L. Gardette, S. Guillerez, N. Lemaître, *Polym. Degrad. Stab*. 2009, **94**, 898
37 Y. Gao, J. K. Grey, *J. Am. Chem. Soc*. 2009, **131**, 9654
38 J. P. Yasomanee, J. Bandara, *Sol. Energ. Mat. Sol. Cells* 2008, **92**, 348; R. L. Smith, G. S. Rohrer, *J. Solid State Chem*. 1996, **124**, 104
39 V. S. Saji, C.-W. Lee, *ChemSusChem* 2012, **5**, 1146
40 a) S. Hu, M. R. Shaner, J. A. Beardslee, M. Lichterman, B. S. Brunschwig, N. S. Lewis, *Science* 2014, **344**, 1005; b) S. Obuchovsky, I. Deckman, M. Moshonov, T. Segal Peretz, G. Ankonina, T. J. Savenije, G. L. Frey, *J. Mater. Chem. C* 2014, **2**, 8903
41 M. T. Greiner, M. G. Helander, W.-M. Tang, Z.-B. Wang, J. Qiu, Z.-H. Lu, *Nat Mater* 2012, **11**, 76
42 S. Esiner, H. Van Eersel, M. M. Wienk, R. A. J. Janssen, *Adv. Mater*. 2013, **25**, 2932